RESEARCH ARTICLE SUMMARY

MOLECULAR BIOLOGY

# Autoinhibition imposed by a large conformational switch of INO80 regulates nucleosome positioning

Upneet Kaur†, Hao Wu†, Yifan Cheng*, Geeta J. Narlikar*

Full article and list of author affiliations: https://doi.org/10.1126/science.adr3831

**INTRODUCTION:** The packaging of eukaryotic DNA into nucleosomes occludes access to the underlying DNA. A primary mechanism for regulating access to DNA is through the rearrangement of nucleosomes by adenosine 5′-triphosphate (ATP)–dependent chromatin remodelers. There are several classes of remodelers, with each class catalyzing a specific set of nucleosome rearrangements. The chromatin remodeler INO80 is critical for precisely positioning nucleosomes near sites of transcription initiation and origins of DNA replication. In vitro, INO80 displays a switch-like response to the length of DNA flanking a nucleosome such that increasing the length from 40 to 80 base pairs (bp) results in ~100-fold faster nucleosome sliding. This property helps explain INO80's ability to precisely position nucleosomes in vivo. However, the mechanistic basis for the tight regulation of INO80's activity by flanking DNA length remains elusive.

**RATIONALE:** INO80 is a multisubunit complex, within which groups of subunits are organized as biochemically separable modules. Existing cryo-EM structures of INO80 on nucleosomes with long flanking DNA show one of these modules, the Arp8 module together with the helicase-SANT–associated (HSA) region of the Ino80 adenosine triphosphatase (ATPase) bound to flanking DNA. Such observations have led to the model that the Arp8 module stimulates INO80 remodeling by helping the HSA region act as a ruler to sense flanking DNA length. To test this role of the Arp8 module, we used cryo–electron microscopy (cryo-EM) to compare the structures of INO80 bound to nucleosomes with 40 bp of flanking DNA (0/40) with those of INO80 bound to nucleosomes with 80 bp of flanking DNA (0/80). We further tested the functional effects of the Arp8 module by either deleting the entire Arp8 module or by targeted mutations in the N-terminal region of the Arp8 subunit. The combination of these structural and biochemical approaches has allowed us to uncover a new role for the Arp8 module in the flanking DNA length sensitivity displayed by INO80.

**RESULTS:** Our cryo-EM structure of INO80 bound to 0/40 nucleosomes revealed that the Arp8 module adopts a distinct autoinhibited conformation, rotating 180° away from flanking DNA. This conformation occludes the HSA from interacting with the flanking DNA, providing an explanation for slower nucleosome sliding. When the flanking DNA length is increased to 80 bp, the Arp8 module gets released from the inhibited conformation, allowing the HSA to interact with flanking DNA. Deletion of the entire Arp8 module or just mutation of the negatively charged N terminus of Arp8 enables rapid sliding of 0/40 nucleosomes, effectively equalizing sliding rates of 0/40 and 0/80 nucleosomes. These results reveal that the Arp8 module does not enable a ruler-like mechanism but rather acts as a brake to inhibit INO80's sliding activity when the flanking DNA is short. We also uncovered an additional conformational state on 0/80 nucleosomes in which the Arp8 module is conformationally dynamic. Our biochemical data suggest that this additional state represents an activated intermediate that is on path for rapid remodeling.

**CONCLUSION:** Our results highlight how a multisubunit chromatin remodeler utilizes its subunits to impose autoinhibition in a manner that is regulated by nucleosomal cues. We speculate that the tunability of INO80's flanking DNA length dependence allows for rapid decrowding of nucleosomes during DNA damage. This property also explains how INO80 precisely positions nucleosomes during replication and transcription. □

*Corresponding author. Email: yifan.cheng@ucsf.edu (Y.C.); geeta.narlikar@ucsf.edu (G.J.N.) †These authors contributed equally to this work. **Cite this article as U. Kaur *et al.*, *Science* 389, eadr3831 (2025). DOI: 10.1126/science.adr3831**

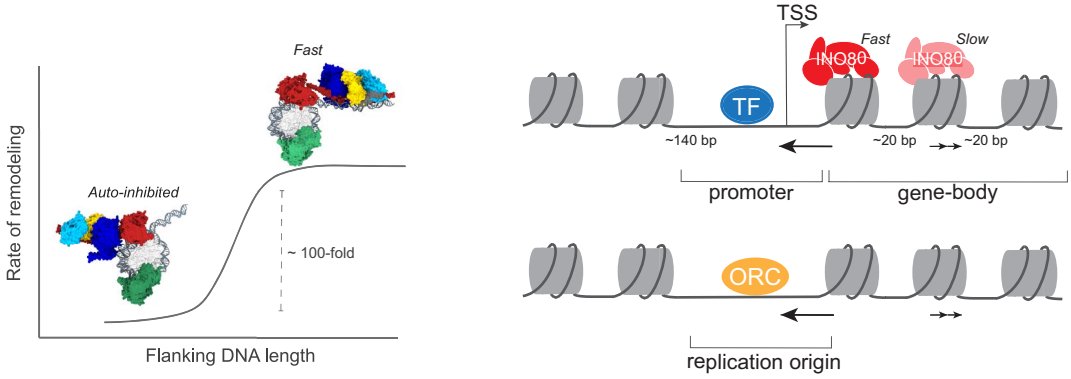


**INO80's switch-like response to flanking DNA is gated by conformational switching of the Arp8 module.** This conformational rearrangement sheds light (left panel) on how INO80 spaces nucleosomes in collaboration with transcription factors (TFs) at transcription start sites (TSS) and the origin recognition complex (ORC) at replication origins (right panel).

MOLECULAR BIOLOGY

# Autoinhibition imposed by a large conformational switch of INO80 regulates nucleosome positioning

Upneet Kaur[1,2]†, Hao Wu[1]†, Yifan Cheng[1,3]*, Geeta J. Narlikar[1]*

Increasing the flanking DNA from 40 to 80 base pairs (bp) causes ~100-fold faster nucleosome sliding by INO80. A prevalent hypothesis posits that the Arp8 module within INO80 enables a ruler-like activity. Using cryogenic electron microscopy, we show that on nucleosomes with 40 bp of flanking DNA, the Arp8 module rotates 180° away from the DNA. Deleting the Arp8 module enables rapid sliding irrespective of flanking DNA length. Thus, rather than enabling a ruler-like activity, the Arp8 module acts as a brake on INO80 remodeling when flanking DNA is short. This autoinhibition–based mechanism has broad implications for understanding how primitive nucleosome mobilization enzymes may have evolved into sophisticated remodelers.

The packaging of eukaryotic DNA into chromatin enables regulation of the core processes that occur on DNA such as transcription, replication, and repair (*1*, *2*). At a fundamental level such regulation occurs through nucleosomes, which are the primary units of chromatin, consisting of ~147 base pairs (bp) of DNA wrapped around an octamer of histone proteins (*3*). Defined positions of nucleosomes enable site-specific initiation of transcription and replication by exposing certain factor binding sites and occluding others. Transcription in *Saccharomyces cerevisiae* (*S.c*) is one of the contexts where the role of nucleosome positioning has been best studied (*4*). The promoters of *S.c* genes exhibit a stereotypical nucleosome positioning pattern consisting of a nucleosome-depleted region (NDR) of ~140 bp flanked by two well-positioned nucleosomes, one upstream (−1 position) and one downstream (+1 position) of the transcription start site (TSS) (*5*, *6*). The nucleosomes within the gene body are spaced with ~20 bp of linker DNA. Defects in this nucleosome organization are associated with cryptic transcription (*7*). Substantial previous work has shown that different conserved classes of adenosine 5′-triphosphate (ATP)–dependent chromatin remodelers collaborate to generate the nucleosome organization at *S.c* promoters. However, among these remodelers, the INO80 chromatin remodeler appears largely sufficient to generate the well-positioned +1 and −1 nucleosomes (*8*–*11*). How INO80 achieves such precise positioning is a matter of active study.

Two types of findings have provided some insight into how *S.c* INO80 regulates nucleosome positions at promoters. One set of findings suggests a role for DNA shape and mechanics for regulating INO80's activity. (*10*). Another set of findings has shown that the nucleosome sliding activity of INO80 is strongly dependent on the length of the DNA flanking a nucleosome (*12*, *13*). INO80 slides nucleosomes with 40 bp of flanking DNA ~100-fold slower than nucleosomes with 80 bp of flanking DNA, displaying a switch-like response to flanking DNA length (*12*). This feature of INO80 can explain why INO80 does not slide the +1 nucleosome into the gene body or the −1 nucleosome into the upstream region. However, the mechanistic basis for this tight regulation by flanking DNA length remains poorly understood.

Testable hypotheses about how flanking DNA length sensing is achieved can be derived from INO80's subunit organization. *S.c* INO80 is a multisubunit complex consisting of 15 subunits that are divided into three different modules (Fig. 1A) (*14*). The core module (C-module) contains the RecA lobes and insert of the Ino80 ATPase and the Arp5, Ies6, Ies2, Rvb1, and Rvb2 subunits. The Arp8 module (Arp8, Arp4, Actin, Ies4, and Taf14) interacts with the helicase-SANT–associated (HSA) region of Ino80. The Nhp10 module (Nhp10, Ies1, Ies3, and Ies5) interacts with the N-terminal region of Ino80. Structural analysis of INO80 bound to nucleosomes with ~80 bp of DNA has shown that the HSA region and the structured regions of the Arp8 module bind ~40 bp of flanking DNA with the possibility that the unstructured regions of the Arp8 module and the flexible Nhp10 module bind additional flanking DNA that is not visualized (*10*, *15*, *16*). These studies have led to the model that the HSA acts as a ruler to sense flanking DNA length and that the Arp8 module stabilizes the interaction of the HSA on DNA (*10*, *11*, *17*). This model predicts that the Arp8 module will be less stably engaged with flanking DNA when it is 40 bp versus 80 bp.

Here, we tested this hypothesis by determining cryo–electron microscopy (cryo-EM) structures of INO80 on nucleosomes with 40 bp (0/40) and 80 bp of flanking DNA (0/80). We find that the Arp8 module, rather than binding less stably to 40 bp of flanking DNA, reorients to a new stable conformation that is ~180° away from the flanking DNA. Deleting the Arp8 module substantially increases sliding of 0/40 nucleosomes, revealing that the Arp8 module plays an unusual autoinhibitory role. Overall, our findings show how autoinhibition can impose a switch-like response to flanking DNA length by a chromatin remodeling complex.

## RESULTS

### Arp8 module shows a large conformational change as a function of flanking DNA length

We first recapitulated previous observations and found that as published, INO80 displayed a large decrease (~100-fold) in remodeling rate when the flanking DNA decreased from 80 to 40 bp on nucleosomes assembled using *Xenopus laevis* (*X.l*) histones and the 601 Widom nucleosome positioning sequence (Fig. 1B) (*12*, *18*). The 601 sequence was used to precisely position nucleosomes and increase the homogeneity of the substrate to enable structural analysis and quantification of remodeling kinetics. In addition, we have previously shown that INO80 slides nucleosomes assembled on the native 5*S* sequence with overall kinetics comparable to those assembled on the 601 sequence (*12*). Remodeling was measured using a well-established INO80 activity assay that followed the movement of an end-positioned nucleosome toward the center of the DNA (fig. S1A and Fig. 1B) (*12*). In earlier structures of INO80 bound to nucleosomes containing ~80 bp of flanking DNA (0/80), the Arp8 module was shown to bind ~40 bp of flanking DNA (*15*, *19*). These findings raised the possibility that the Arp8 module contributes to flanking DNA length sensing by helping the HSA act as a ruler (*11*). Our more recent structure of *S.c* INO80 on 0/80 nucleosomes in the apo state (no nucleotide bound) for Ino80 also shows the Arp8 module bound to ~40 bp of flanking DNA (*20*). To assess whether the nucleotide state affected the location of the Arp8 module, we determined structures of *S.c* INO80 on 0/80 and 0/40 nucleosomes in the presence of a nonhydrolyzable ATP analog (ADP/$BeF_x$).

The overall structure of INO80 bound to 0/80 nucleosomes in the presence of ADP/$BeF_x$ is similar to the previously published structure in the apo state (Fig. 1C and fig. S1) (*20*). The INO80 C-module is well resolved at a resolution of 2.8 Å. The RecA1 lobe is less resolved compared with the RecA2 lobe, presumably adopting an open conformation where the ATPase lobes are not stably bound to nucleotide (fig. S2). The Arp8 module is resolved as a well-defined density on the flanking

[1]Department of Biochemistry and Biophysics, University of California San Francisco, San Francisco, CA, USA. [2]Biophysics Graduate Program, University of California San Francisco, San Francisco, CA, USA. [3]Howard Hughes Medical Institute, University of California San Francisco, San Francisco, CA, USA. ***Corresponding author. Email: yifan.cheng@ucsf.edu (Y.C.); geeta.narlikar@ucsf.edu (G.J.N.)** †These authors contributed equally to this work.

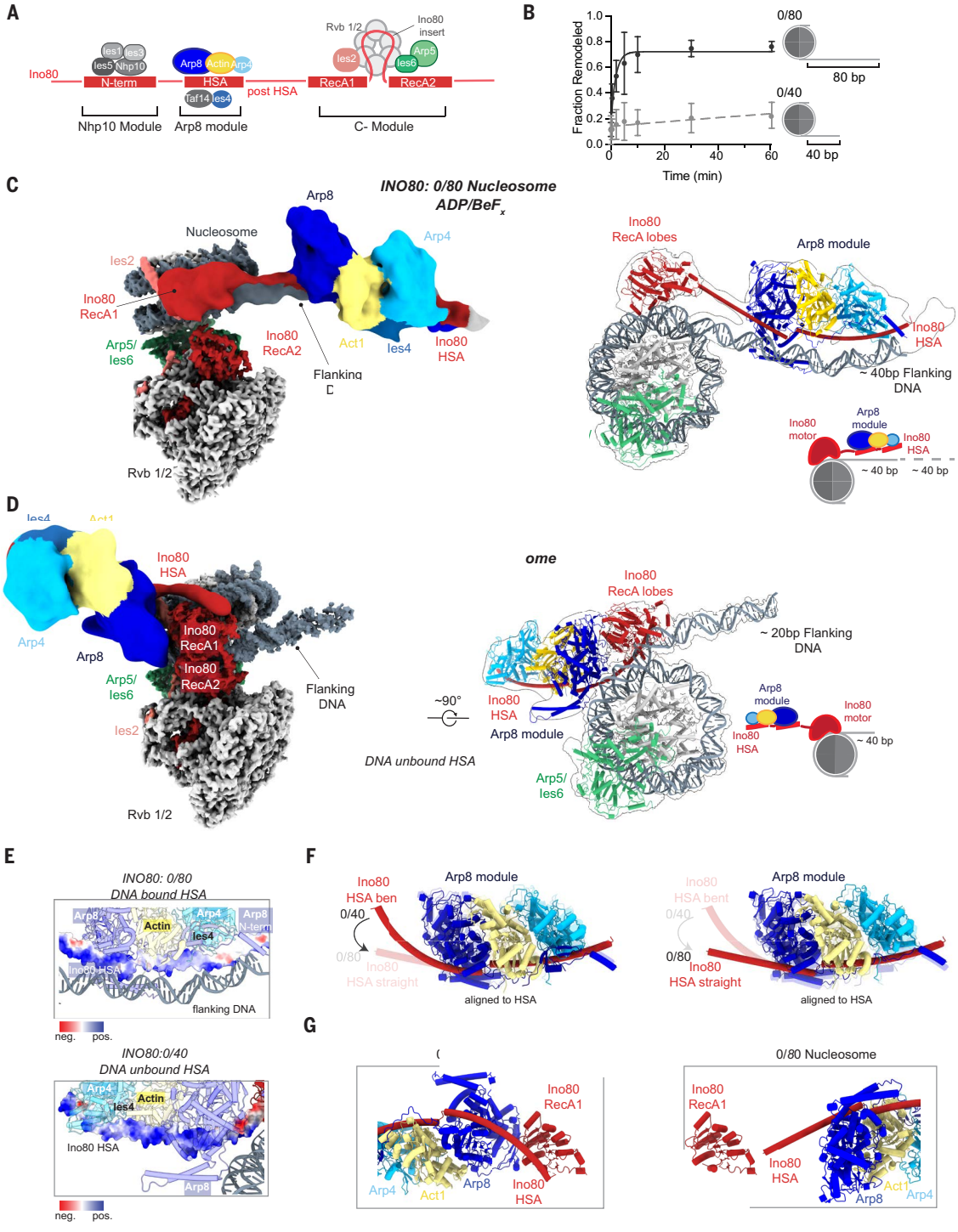


**Fig. 1. Structural rearrangement of the Arp8 module switches INO80 from an inactive to an active state.** (**A**) ATPase architecture and module assembly of the INO80 complex. (**B**) Quantification of fraction product from native gel-based remodeling assays of INO80 on 0/80 (black) and 0/40 (dashed gray) nucleosomes shown in fig. S1A. Error bars represent SD for three technical replicates. (**C**) Cryo-EM density composite map of INO80-0/80 *X.I* nucleosome complex in the presence of ADP/BeF$_x$ (left). Atomic model of the map shown in the left panel in a 90° rotated view with map outline of Ino80 recA lobes and HSA, Arp5/Ies6, and Arp8 module bound to the nucleosome (right). The Rvb1/2 and Ies2 subunits are not shown in the right panel for clarity. In the accompanying cartoon, the RecA lobes are denoted as the Ino80 motor. Atomic model of the Arp8 module was docked in from a previously determined structure (PDB: 8A50). (**D**) Cryo-EM density composite map of INO80-0/40 *X.I* nucleosome complex in the presence of ADP/BeF$_x$ (left). Atomic model of the map shown in the left panel in a 90° rotated view with map outline of Ino80 RecA lobes and HSA, Arp5/Ies6, and Arp8 module bound to the nucleosome (right). The Rvb1/2 and Ies2 subunits are not shown in the right panel for clarity. Atomic model of the Arp8 was docked in from a previously determined structure (PDB: 8A50). (**E**) Surface charge distribution of the HSA region in Ino80 that interacts with the flanking DNA on 0/80 nucleosomes (top panel) or is DNA unbound on 0/40 nucleosomes (bottom panel). The HSA is colored according to the coulombic electrostatic potential. (**F**) Bending of the HSA with 0/40 nucleosomes to straightening with 0/80 nucleosomes, both in the ADP/BeFx state. The 0/40 state is highlighted in the left panel and the 0/80 state in the right panel. (**G**) Comparison of the RecA lobe1 and HSA conformation for 0/40 (left panel) and 0/80 nucleosomes (right panel) in the ADP/BeF$_x$ state.

DNA (~40 bp). Although at a lower resolution (~11.2 Å), we can dock the previously published atomic model of the *S.c* Arp8 module bound to the HSA region of the ATPase into this density (*15*).

However, the INO80 structure on 0/40 nucleosomes revealed some large differences. The overall architecture of the C-module of INO80 bound to 0/80 and 0/40 nucleosomes is similar, except that with 0/40 nucleosomes the RecA lobes are in a closed conformation and stably bound to ADP/$BeF_x$ (Fig. 1D and fig. S3). The most substantial difference in the structure is the location of the Arp8 module as detailed below. Although the flanking DNA is partially resolved in the same orientation as seen on 0/80 nucleosomes, no additional density was seen on the flanking DNA. Instead, additional density is observed around the Ino80 RecA lobes that is absent in the 0/80 nucleosome structure. Further focused classification and local refinement of this density (~9.7 Å) revealed a clearly defined structural feature to be compatible with the Arp8 module. The previously determined atomic model of the Arp8 module bound to the HSA could be docked into this density and revealed that the Arp8 module on 0/40 nucleosomes rotates ~180° compared to the Arp8 module on 0/80 nucleosomes (movie S1). The region that connects the HSA to the RecA lobes is termed the post-HSA and is not well resolved in structures of INO80 bound to 0/80 or 0/40 nucleosomes. However, this region is predicted to include disordered regions and could allow the large rearrangement of the Arp8 module (fig. S4) (*21*). Thus, on 0/40 nucleosomes, the Arp8 module and HSA no longer contact the flanking DNA (Fig. 1D). The HSA region of Ino80 consists of multiple positively charged residues that are implicated to play important roles in binding to flanking DNA and in nucleosome sliding (*10*, *15*) (Fig. 1E). On the 0/40 nucleosomes, the reorientation of the HSA disengages it from DNA, potentially leaving the positively charged interface solvent exposed, which we discuss below (Fig. 1E). The overall shape of the Arp8 module is well resolved and similar in both the 0/80 and 0/40 cryo-EM maps. Overlaying the Arp8 module reveals that the HSA in the 0/40 structure is bent compared with the 0/80 structure (Fig. 1F). Specifically, a region of the HSA undergoes a conformational shift from being near the RecA1 lobe in the 0/40 structure to being extended when interacting with the flanking DNA in the 0/80 structure (Fig. 1G).

### Enhanced activity on *S.c* 0/80 nucleosomes correlates with increased dynamics of the Arp8 module

The drastic rearrangement of the Arp8 module suggested that its location may correlate with the activity of INO80. We hypothesized that on 0/40 nucleosomes, the location of the Arp8 module represents an inhibited conformation of INO80. By contrast, on 0/80 nucleosomes, where the Arp8 module engages the flanking DNA, this location of the Arp8 module potentially represents a sliding-competent state of INO80. Note that all published biochemical and structural studies of the *S.c* INO80 have been performed with nucleosomes containing non-*S.c* histones. Although histone proteins are highly conserved among eukaryotes, *S.c* histones are the most divergent from *X.l* and *Homo sapiens* (*H.s*) histones (fig. S5) (*22*). To test whether the reorientation of the Arp8 module was dependent on the species of histones used, we performed biochemical and structural studies of INO80 on nucleosomes containing *S.c* histones assembled on the 601-nucleosome positioning sequence (*S.c* nucleosomes) with either 80 or 40 bp of flanking DNA.

Generating large amounts of *S.c* H4 was technically challenging. Given the high conservation between *S.c* and *X.l* H4, we tested the effects of using *X.l* H4 instead of *S.c* H4 (fig. S5). We found that the remodeling rates of nucleosomes containing all *S.c* histones were within 2-fold of remodeling rates containing *S.c* H2A, H2B, H3, and *X.l* H4 (fig. S6, A and B). Therefore, for all experiments except those in fig. S6, we used *X.l* H4 instead of *S.c* H4 to make *S.c* nucleosomes as generating large amounts of *X.l* H4 is technically feasible. When remodeling reactions were performed at 30°C, our standard remodeling conditions and the optimal growth temperature of budding yeast, we found that INO80 centered *S.c* 0/80 nucleosomes rapidly, making it difficult to measure the kinetics (fig. S6C). The remodeling of *S.c* 0/80 nucleosomes went to near completion (>3 halftimes) within 15 s compared with remodeling *of X.l* 0/80 nucleosomes that went to near completion in 2 min. To more quantitatively compare INO80's remodeling kinetics on *S.c* 0/80 and *X.l* 0/80 nucleosomes, the reaction was either performed at 10°C or with subsaturating ATP to slow down the rate of remodeling. Under these conditions, we found that INO80 remodeled *S.c* 0/80 nucleosomes 45-fold faster compared to *X.l* nucleosomes (Fig. 2, A and B). Given INO80's enhanced activity on *S.c* nucleosomes, we explored whether flanking DNA remains a crucial substrate cue for INO80 on *S.c* nucleosomes. Shortening the flanking DNA from 80 to 40 bp for *S.c* nucleosomes reduced the remodeling rate of INO80 by ~100-fold (fig. S6, D and E). This suggested that length sensing was not dependent on the species of histones but rather is a core feature of INO80's sliding mechanism.

Our results raised the question of why *S.c* nucleosomes are better substrates than *X.l* nucleosomes. There are differences in the sequences of H2A, H2B, H3, and H4 between *S.c* and *X.l* (fig. S5). As mentioned above, substituting *S.c* H4 for *X.l* H4 does not have a large effect on INO80's remodeling activity (fig. S6, A and B). We therefore explored the effects of varying H2A, H2B, and H3. We first tested the effects of differences between the H2A and H2B sequences. Replacing the *X.l* H2A-H2B in *X.l* nucleosomes with *S.c* H2A-H2B resulted in 7-fold faster remodeling by INO80. Although the overall structure of *S.c* nucleosomes is similar to that of *X.l* nucleosomes, a key difference is the interaction between the two H2A-H2B dimers (*22*). In *X.l* nucleosomes, the two H2A-H2B dimer copies interact through a series of salt-bridges between the H2A histones (fig. S7A). These salt bridges are absent in *S.c* nucleosomes and may contribute to weaker interactions between the two copies of the dimer (*22*). In previous work, subtle conformational rearrangements of the H2A-H2B dimers have been suggested to be important for INO80 to achieve a sliding-competent state (*20*). Thus, the faster remodeling that we observed with replacing *X.l* H2A-H2B in *X.l* nucleosomes with *S.c* H2A-H2B could arise because of the potentially weaker dimer interactions in *S.c* nucleosomes. However, this result also implied that not all of the ~50-fold rate enhancement derives from differences in the H2A-H2B dimer. We then asked if differences between the *X.l* and *S.c* H3-H4 tetramers also played a role in differential remodeling by INO80. Replacing *X.l* H3 with *S.c* H3 led to ~7-fold faster remodeling by INO80. These results indicated that the difference in sequence between *X.l* H3 and *S.c* H3 also contributes to faster remodeling by INO80 (fig. S6, F and G). One explanation arises from inspection of the structure of INO80 bound to nucleosomes, which implies contacts between specific aspartate residues of the Arp5 subunit (D547 and D551) and residues 121 and 125 of H3 (α3 helix) (fig. S7B). In *X.l* H3, these residues are P121 and Q125, whereas in *S.c* H3 these are K121 and K125. We speculated that the potentially stronger electrostatic interactions made in the context of *S.c* H3 may enable INO80 to more readily hold on to the nucleosome during the conformational transitions required for remodeling. Overall, the effects were additive in terms of free energy (7-fold × 7-fold = 49-fold) and indicated that the ~50-fold rate enhancement requires *S.c*-specific H2A-H2B dimer interactions and *S.c*-specific H3 interactions.

The enhanced remodeling activity of INO80 on *S.c* 0/80 nucleosomes provided an opportunity to test whether and how the conformation of the Arp8 module changed on these nucleosomes compared with *X.l* 0/80 nucleosomes as a function of nucleotide state. For *X.l* nucleosomes, no major difference is observed between the previously published structure in the apo state and the structure determined here in the presence of ADP/$BeF_x$ (Fig. 2, C and D), suggesting that the nucleotide state does not significantly influence the Arp8 module's conformation on *X.l* nucleosomes. With *S.c* 0/80 nucleosomes, we

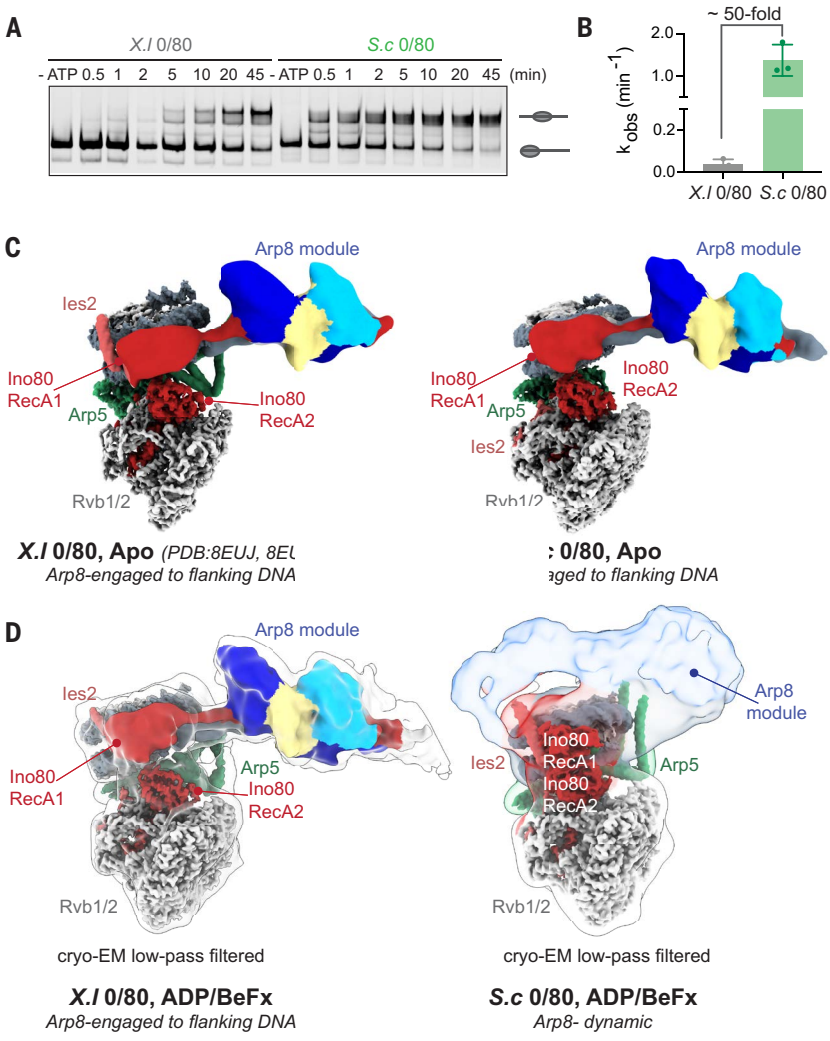


**Fig. 2. Enhanced activity of INO80 on *S.c* nucleosomes correlates with increased dynamics of the Arp8 module.** (**A**) Native gel-based remodeling assay of INO80 on *X.l* and *S.c* 0/80 nucleosomes at 10°C. Substrates (end-positioned nucleosomes and center-positioned nucleosomes) are labeled by illustrations next to the respective bands in gels. (**B**) Quantification of rate constants from three repeats of data shown in (A). Error bars represent SD for three technical replicates. (**C**) Cryo-EM composite maps of INO80 bound to either *X.l* 0/80 nucleosomes (left panel) or *S.c* 0/80 nucleosomes (right panel) in the apo state. The *X.l* 0/80 composite map is from a previously published structure (PDB: 8EUJ and 8EUF). (**D**) Cryo-EM composite maps of INO80 bound to either *X.l* 0/80 nucleosomes (left panel) or *S.c* 0/80 nucleosomes (right panel) in the ADP/$BeF_x$ state. The map resultant of the low-pass filter applied to either *X.l* or *S.c* 0/80 nucleosomes is shown as transparent. The left panel map is the same as shown in Fig. 1C (left panel) and is reshown here for ease of comparison.

see larger differences between the structures in the apo and ADP/$BeF_x$ states. In both states, the C-module of INO80 bound to *S.c* nucleosomes adopts an architecture similar to that seen with *X.l* 0/80 nucleosomes (Fig. 2, C and D, and figs. S8 and S9). Further, in the ADP/$BeF_x$ state, the RecA lobes are in a closed conformation and stably bound to ADP/$BeF_x$, whereas in the Apo state, the RecA lobes are in an open conformation. However, the major difference between these structures is the location of the Arp8 module. In the apo state of INO80 on *S.c* 0/80 nucleosomes, we detected well-defined density for the Arp8 module on flanking DNA similar to what was detected previously for the apo state on *X.l* 0/80 nucleosomes. By contrast, in the presence of ADP/$BeF_x$, the density for the Arp8 module is less distinct, suggesting that the engagement of the Arp8 module with flanking DNA is more dynamic in this nucleotide-bound state. In comparison, the cryo-EM structure of INO80 bound to 0/40 *S.c* nucleosomes in the ADP/$BeF_x$ state showed that the Arp8 module adopts a conformation similar to that observed on 0/40 *X.l* nucleosomes in the ADP/$BeF_x$ state (figs. S10 to S12). Two distinct classes were identified in this dataset for 0/40 *S.c* nucleosomes, with the grappler region of Arp5 adopting either a crossed or parallel conformation (fig. S11). These conformations have also been observed for INO80 bound to 0/80 nucleosomes, but the functional consequence of these conformations has not been identified (*19*).

Together these data suggested that on 0/80 nucleosomes, INO80 adopts conformational states that range from the Arp8 module stably bound to flanking DNA to a more dynamic Arp8 module. To better assess this range of conformational states and identify the minor conformations with few particles that would be missed by standard cryo-EM classification, we performed three-dimensional (3D) classification by mixing datasets of INO80 bound to *X.l* 0/80, *S.c* 0/80, *X.l* 0/40, and *S.c* 0/40 in the ADP/BeFx state (fig. S13). This mixed dataset also included a dataset of a mutant INO80 complex bound to *S.c* 0/40 in the ADP/BeFx state, described later in the text. Particles of each class were then traced back to the original sample to obtain appropriate particle distributions among different classes in each dataset. This approach provided a better chance for identifying conformations that are populated to a small extent in one dataset but more populated in another dataset. This analysis identified four classes based on clear or partial density of the Arp8 module: (i) a class with clear density for the Arp8 module rotated away from the flanking DNA (class 1a); (ii) a class with partial density for the Arp8 module rotated away from the flanking DNA (class 1b); (iii) a class with clear density for the Arp8 module bound to flanking DNA (class 2a); and (iv) a class with partial density for the Arp8 module bound to flanking DNA (class 2b). The remaining particles did not show any density for the Arp8 module and were grouped into a fifth class (class 3).

This analysis revealed that in the INO80–*S.c* 0/40 (ADP/$BeF_x$) and INO80–*X.l* 0/40 (ADP/$BeF_x$) datasets, a majority of the particles showed either clear or partial density for the Arp8 module held away from flanking DNA (classes 1a and 1b) (fig. S13). In comparison, for the INO80–*S.c* 0/80 (ADP/$BeF_x$) and INO80–*X.l* 0/80 (ADP/$BeF_x$) datasets, a much smaller proportion of particles fell in classes 1a and 1b. It is further informative that, for the INO80–*S.c* 0/40 (ADP/$BeF_x$) and INO80–*X.l* 0/40 (ADP/$BeF_x$) complexes, only a small proportion of particles have either clear or partial density for the Arp8 module on the flanking DNA. These results suggest that on 0/40 nucleosomes, the equilibrium of INO80 is more biased toward a state in which the Arp8 module is held away from the flanking DNA.

We further find that for the INO80–*X.l* 0/80 (ADP/$BeF_x$) sample, a majority of the particles have clear or partial density for the Arp8 module on flanking DNA (classes 2a and 2b), and a small proportion do not show density for the Arp8 module (class 3) (fig. S12). By contrast, for the INO80–*S.c.*0/80 (ADP/$BeF_x$) dataset, the majority of the particles do not show density for the Arp8 module (class 3) and a small minority show clear or partial density for the Arp8 module on flanking DNA (classes 2a and 2b). These data suggest that on *S.c* 0/80 nucleosomes, as compared to *X.l* 0/80 nucleosomes, a greater proportion of INO80 adopts a state in which the Arp8 module is more dynamic.

### The Nhp10 and Arp8 module cooperate to impose flanking DNA length dependence

Previous studies have suggested that the Arp8 module activates remodeling by stabilizing binding of the HSA to flanking DNA (*10*, *11*, *15*, *17*). However, our structures with the *S.c* 0/80 nucleosomes suggested instead that a conformationally dynamic Arp8 module correlates with greater INO80 activity. These findings made us question the Arp8 module's proposed role. To more directly assess the functional contribution of the Arp8 module, we tested the effects of deleting this module.

INO80 complexes lacking the Arp8 module (ΔArp8) were purified from yeast strains lacking the Arp8 subunit, which results in the absence of the entire module (fig. S14). The activity of ΔArp8 INO80 was tested on *S.c* 0/80 and 0/40 nucleosomes. Deletion of the Arp8 module resulted in only a moderate decrease (~2-fold) in sliding of *S.c* 0/80 nucleosomes. By contrast, this deletion resulted in a ~75-fold increase in remodeling of *S.c* 0/40 nucleosomes (Fig. 3, A and B). These results indicated that the Arp8 module slows the sliding of nucleosomes with shorter flanking DNAs rather than substantially activating sliding of nucleosomes with longer flanking DNA length. Thus, the Arp8 module plays an autoinhibitory role on 0/40 nucleosomes. As a result, in the absence of the Arp8 module, INO80 remodeled both 0/40 and 0/80 nucleosomes rapidly and with comparable kinetics, and the sliding activity of INO80 was not dependent on flanking DNA length.

Our structures with 0/40 nucleosomes suggest that the Arp8 module sequesters the HSA away from flanking DNA, thereby inhibiting its ability to bind flanking DNA. This raised the question of how the location of the Arp8 module is regulated as a function of flanking DNA length. We observed additional density proximal to the Arp8 module in a low pass–filtered map of INO80 bound to 0/40 nucleosomes, which covers the positively charged residues of the HSA on 0/40 nucleosomes (Fig. 3C). This additional density could be compatible with the Nhp10 module, which interacts with the N terminus of Ino80. The Nhp10 module, which contains DNA binding domains, has not been structurally characterized as it also contains many disordered segments (*23*). However, deletion of this module has been shown to increase remodeling of *X.l* 0/40 nucleosomes by ~100-fold, a result we also observed with *S.c* 0/40 nucleosomes (fig. S15A) (*12*). This suggested that the Arp8 and Nhp10 modules both play a role in autoinhibition (Fig. 3D). To test whether these two modules cooperate, we investigated the effects of deleting both modules on INO80's sliding activity. The ΔArp8/Nhp10 complex displayed a slight decrease (~3-fold) in sliding of 0/80 nucleosomes but increased the remodeling of 0/40 nucleosomes by ~60-fold (Fig. 3, A and B). Because deleting both modules had an effect comparable to that of deleting either module, we concluded that the Nhp10 and Arp8 modules cooperate to sequester the HSA from flanking DNA on 0/40 nucleosomes.

How might these two modules cooperate? We hypothesized that the cooperation occurs through the N terminus of Arp8. This region of Arp8 contains several negatively charged residues that could substitute for the interactions made by the flanking DNA with the HSA. Interactions by these negatively charged residues could be distributed between the positively charged HSA, sequestering it from binding DNA and the DNA binding regions of the Nhp10 module, resulting in a stably inhibited state (Fig. 3E). To test this model, we generated INO80 complexes that lacked the N terminus of Arp8 (1–197) while retaining the rest of the Arp8 module as previously reported (fig. S14) (*17*). Similar to the results with ΔArp8 INO80, an ~100-fold increase in the remodeling rate of 0/40 nucleosomes was observed using ΔN-Arp8 INO80 (Fig. 3, F and G). However, in contrast to ΔArp8 INO80, which exhibited a slight decrease (~2-fold) in the remodeling rate of 0/80 nucleosomes, ΔN-Arp8 INO80 remodeled 0/80 nucleosomes with a rate similar to that of WT INO80. These results indicated that deleting the Arp8 N terminus more specifically removed the autoinhibitory role of the Arp8 module as this did not affect remodeling of 0/80 nucleosomes. To more directly test the effect of the negatively charged residues in the N terminus of Arp8, we mutated the aspartic and glutamic acid residues highlighted in Fig. 3E to glycine and serine residues. We refer to this mutant as Arp8-acidic mutant (Arp8-AM). Similar to ΔN-Arp8 INO80, Arp8-AM INO80 retained all of the subunits in the Arp8 module (fig. S14). Arp8-AM INO80 also displayed an ~100-fold increase in the remodeling rate of 0/40 nucleosomes without significantly affecting the remodeling rate of 0/80 nucleosomes (Fig. 3, F and G). These experiments highlighted the benefits of targeted mutations compared to whole gene deletions for understanding the mechanisms of multisubunit remodelers such as INO80. Overall, the results were consistent with the model that the negatively charged residues in the N terminus of Arp8 sequester the HSA from binding flanking DNA on 0/40 nucleosomes.

The data above were also consistent with the N terminus of Arp8 cooperating with the Nhp10 module to impose autoinhibition. To explore this possibility from a structural perspective, we determined the cryo-EM structure of ΔNhp10 INO80 bound to 0/40 *S.c* nucleosomes in the presence of ADP/$BeF_x$ (fig. S15). The overall architecture of the C-module of ΔNhp10 INO80 bound to *S.c* 0/40 nucleosomes is again similar to that with *S.c* 0/40 and 0/80 nucleosomes (Fig. 3H, left panel). Through further cryo-EM processing, we find that the majority of particles show undefined density for the Arp8 module similar to the INO80 bound to *S.c* 0/80 nucleosome data set in the ADP/BeFx state. Additionally, we identified a small subset of particles showing the Arp8 module on the flanking DNA (~5%) and another small subset of particles showing the Arp8 module rotated away from the flanking DNA (~4%) (Fig. 3H, center and right panel, respectively). Thus, deleting the Nhp10 module substantially decreased the proportion of INO80 molecules in the inhibited state. These data suggested that without the Nhp10 module, the Arp8 module is released from the inactive conformation and adopts more than one conformation. Our biochemical data further suggested that without the Arp8 module, the Nhp10 module does not play a large role in inhibiting the HSA. To test this possibility structurally, we determined the cryo-EM structure of ΔArp8 INO80 bound to *S.c* 0/40 nucleosomes in the presence of ADP/$BeF_x$ (fig. S16). The overall architecture of the C-module of ΔArp8 INO80 bound to 0/40 nucleosomes is again similar to that observed with WT INO80 bound to *S.c* 0/40 and 0/80. However, the density corresponding to the HSA around the Ino80 motor domain that was observed with the Arp8 module in WT INO80 is no longer detectable (fig. S17). This is likely because, without the Arp8 module, the HSA region is either poorly structured or highly dynamic. We interpret the absence of HSA density as indicative of an activated state, in which the HSA is no longer held in an inactive conformation by the Arp8 module. These results are consistent with the hypothesis that the Nhp10 and Arp8 modules cooperatively inhibit the HSA from contacting flanking DNA on 0/40 nucleosomes.

## DISCUSSION

How INO80 achieves its distinctive switch-like response to flanking DNA length has been unclear. Here, through a collection of structures, we have uncovered a large conformational change of INO80 that converts INO80 from an inhibited conformation to an active conformation when flanking DNA increases to 80 bp. Below we discuss the biochemical model rising from these studies (Fig. 4) and its implications for the biological roles of INO80.

### Regulatory role of the Arp8 module in INO80's mechanism

Previous data have suggested that the Arp8 module senses flanking DNA length to drive nucleosome sliding (*10*, *16*, *17*). However, our results suggest a different role for the Arp8 module. In contrast to the Arp8 module being required for rapid nucleosome sliding, we find that it plays an autoinhibitory role to tune INO80's flanking DNA length dependence. Specifically, we find that deletion of the Arp8

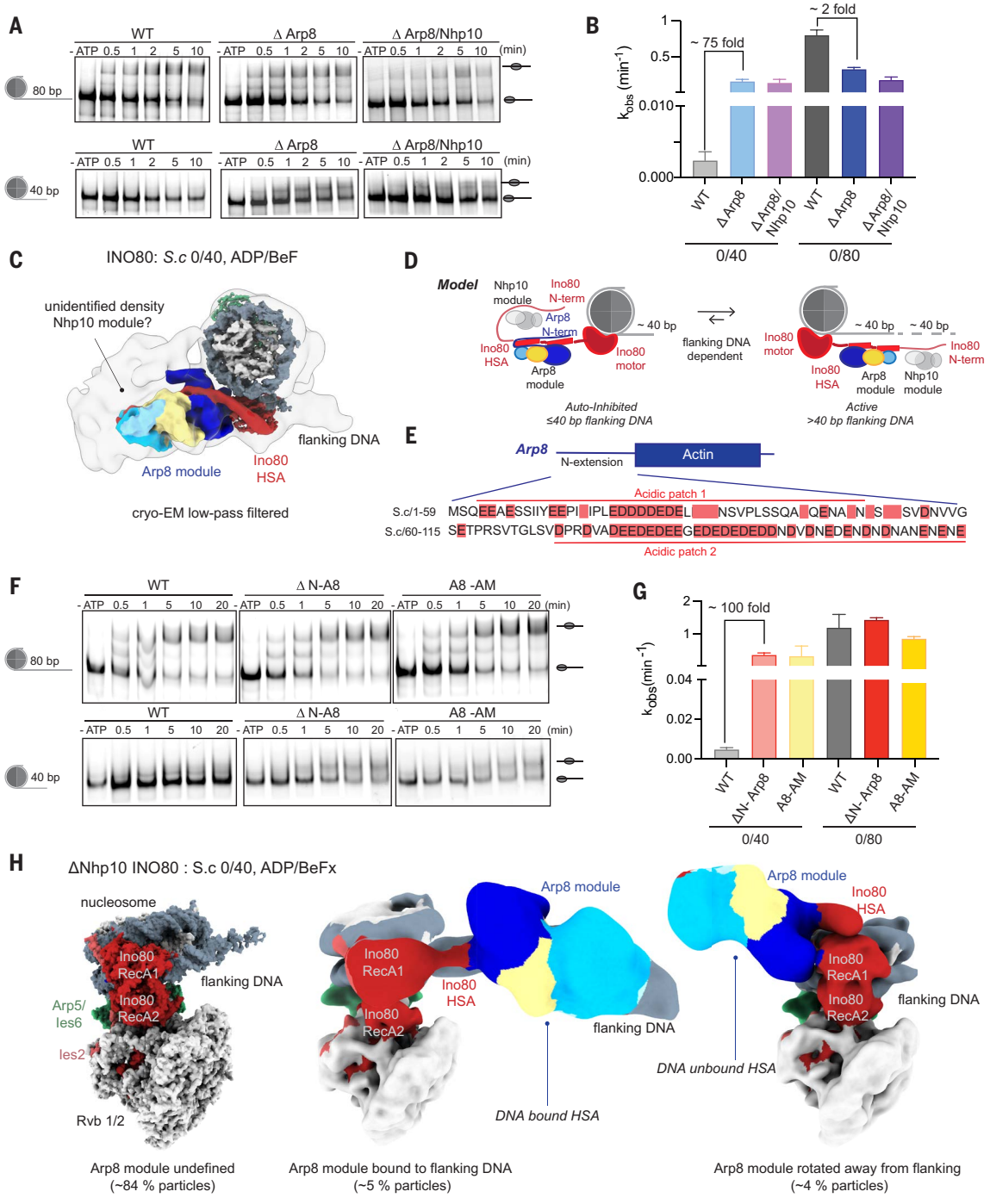


**Fig. 3. The Arp8 and Nhp10 modules collaborate to play an autoinhibitory role in nucleosome remodeling.** (**A**) Native gel-based remodeling assay of WT INO80, ΔArp8 INO80, and ΔArp8/Nhp10 INO80 on *S.c* 0/80 (top panel) and *S.c* 0/40 (bottom panel). Substrates (end-positioned nucleosomes and center-positioned nucleosomes) are labeled by illustrations next to the respective bands in gels. (**B**) Quantification of rate constants from three repeats of data shown in (A). Error bars represent SD for three technical replicates. (**C**) Cryo-EM map of INO80 bound to *S.c* 0/40 nucleosomes only displaying the Ino80 RecA lobes, HSA, and Arp8 module. The other subunits are not shown for clarity. The cryo-EM low pass–filtered map is shown in gray and outlined in black. (**D**) Model depicting potential cooperation of the Nhp10 and Arp8 module to inhibit sliding of INO80 on 0/40 nucleosomes. The N-terminal region of Arp8 is shown as interacting with the HSA and with the Nhp10 module in the context of 0/40 nucleosomes. In the context of 0/80 nucleosomes, this region of Arp8 is not shown as it is unclear what it may interact with. (**E**) Domain architecture of Arp8 showing the N-extension region that contains two major acidic patches of glutamic and aspartic acids. The residues highlighted in salmon are the ones mutated to serines and glycines to generate the Arp8-AM INO80 complex. Single-letter abbreviations for the amino acid residues are as follows: A, Ala; D, Asp; E, Glu; G, Gly; I, Ile; K, Lys; L, Leu; M, Met; N, Asn; P, Pro; Q, Gln; R, Arg; S, Ser; T, Thr; V, Val; and Y, Tyr. (**F**) Native gel-based remodeling assay of WT INO80, ΔN-Arp8 INO80, and Arp8-AM INO80 on *S.c* 0/80 (top panel) and 0/40 (bottom panel). Substrates (end-positioned nucleosomes and center-positioned nucleosomes) are labeled by illustrations next to the respective bands in gels. (**G**) Quantification of rate constants from three repeats of data shown in (F). Error bars represent SD for three technical replicates. (**H**) Cryo-EM map of ΔNhp10 INO80 bound to *S.c* 0/40 nucleosomes in the ADP/$BeF_x$ state. Most of the particles (~84%, left panel) lack defined density of the Arp8 module. A small population of particles were identified in either the state where the Arp8 module is on the flanking DNA (~5%, middle panel) or where the Arp8 module has rotated away from the flanking DNA (~4%, right panel).

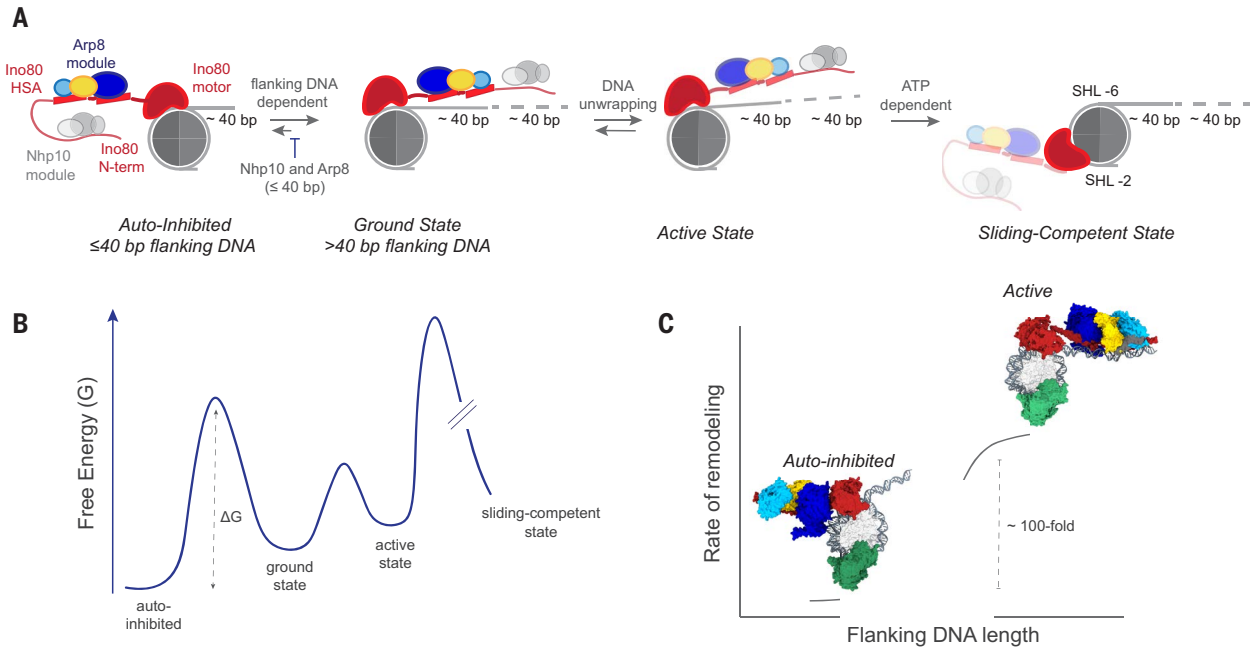


**Fig. 4. Model for flanking DNA length sensing by INO80.** (**A**) INO80 binds 0/40 nucleosomes in an autoinhibited state through cooperation of the Arp8 and Nhp10 modules. When flanking DNA is >40 bp, the Arp8 module and HSA are released from the inhibited state, and the HSA interacts with the flanking DNA representing the ground state. The ground state is in equilibrium with an intermediate state in which the Arp8 module is conformationally dynamic and nucleosomal DNA is unwrapped. The conformationally dynamic Arp8 module allows reorientation of the INO80 complex to a sliding-competent state. (**B**) This model is also depicted in the form of a free energy profile. (**C**) Depiction of INO80's switch-like response to flanking DNA, which is gated by a large conformational change of the Arp8 module. Ino80, Arp5, Arp8, Actin, Arp4, and Ies4 are show in red, green, blue, gold, cyan, and dark gray, respectively.

module greatly (~75-fold) increased the rate of remodeling on 0/40 nucleosomes, with a modest decrease (~ 2-fold) in remodeling of 0/80 nucleosomes. Thus, without the Arp8 module, nucleosome sliding was still rapid and no longer required greater than 40 bp of flanking DNA. On the basis of the structures obtained here, we propose that the Nhp10 and Arp8 modules are in an equilibrium between two states, (i) a state in which the Nhp10 module and Arp8 module interact to inhibit binding of the HSA to flanking DNA and (ii) a state in which the Nhp10 module interacts with additional flanking DNA, releasing the HSA from its inhibited conformation (Fig. 4). On nucleosomes with longer flanking DNA the equilibrium would shift toward the second state and release the HSA from the autoinhibited state. Specifically, our data are consistent with a model in which the negatively charged residues in the N terminus of Arp8 sequester the positively charged HSA from binding flanking DNA. In this model the inhibitory interaction is further stabilized by the Nhp10 module, which carries DNA binding domains. Although the Nhp10 module and the N terminus of Arp8 are not conserved between *S.c* and *H.s* (fig. S18), it is possible that in *H.s*, their roles are served by other, yet to be characterized INO80 subunits.

### Implications of a dynamic Arp8 module in INO80's nucleosome sliding mechanism

The interaction of the Arp8 module and HSA with flanking DNA seen on *X.l* 0/80 nucleosomes is consistent with prior studies implicating the HSA in nucleosome sliding (*15*–*17*). However, the conformational heterogeneity of the Arp8 module on *S.c* 0/80 nucleosomes, which are remodeled ~45-fold faster than *X.l* 0/80 nucleosomes, provides an additional snapshot into INO80's sliding mechanism. We propose that a dynamic and rearranged Arp8 module with DNA unwrapping at the entry site is required for efficient nucleosome sliding by INO80. By this model, the stably bound Arp8 module with the HSA interacting with flanking DNA as seen for *S.c* 0/80 nucleosomes in the Apo state represents a ground state conformation. The activated state is represented by the structure of INO80 on *S.c* 0/80 nucleosomes with ADP/BeFx where more DNA is unwrapped, the Arp8 module adopts additional conformational states, and the RecA lobes are closed. Recently, it has been proposed that INO80 may undergo an ATP-dependent rotation that relocates the Ino80 ATPase from SHL-6 to SHL-2 on a nucleosome to achieve a sliding-competent conformation (*20*). We speculate that such a rotation may require the Arp8 module to be released from flanking DNA, resulting in DNA unwrapping and allowing the movement of the Ino80 ATPase toward SHL-2. The model presented here thus proposes three key steps to initiate nucleosome sliding by INO80: (i) The Arp8 module needs to release the HSA from the inhibited conformation where it cannot access DNA, (ii) the HSA needs to contact the flanking DNA, and (iii) the Arp8 module needs to be conformationally dynamic to allow reorientation of the INO80 complex to a sliding-competent state (Fig. 4). This model can explain why *S.c* nucleosomes are remodeled faster than *X.l* nucleosomes. With *X.l.* 0/80 nucleosomes, the equilibrium is shifted toward the ground state, whereas with *S.c* 0/80 nucleosomes, the equilibrium is shifted toward the activated state. As a result, the overall activation barrier for remodeling of *S.c* nucleosomes is reduced compared to that for *X.l* nucleosomes.

Flanking DNA length sensing is also a feature of remodelers from the ISWI family (*24*). For these remodelers, the rate of remodeling and ATP hydrolysis are both regulated by flanking DNA length (*25*, *26*). By contrast, whereas INO80's remodeling activity is dependent on flanking DNA length, its ATPase activity is independent of flanking DNA length (*12*, *13*). Furthermore, previous data have shown that deletion of the Arp8 or Nhp10 module or mutations in the HSA only affect remodeling activity and not ATPase activity (*10*, *12*, *15*). Thus, unlike ISWI remodelers, the ATPase activity of INO80 is not directly coupled to sensing flanking DNA length. Our model (Fig. 4) provides a framework

to explain this difference. We propose that the Arp8 and Nhp10 modules regulate how well the ATPase activity of Ino80 is coupled to nucleosome sliding in response to flanking DNA length. By doing so, these modules gate the early steps of movement of the Ino80 ATPase from SHL-6 to SHL-2 and make the overall reaction dependent on flanking DNA length.

It is further informative to compare the autoinhibition mechanism uncovered here to autoinhibition mechanisms found in other chromatin remodelers. For ISWI, CHD1, and ALC1 remodelers, the ATPase subunit has been shown to be in the autoinhibited state, and recognition of the appropriate substrate cues on a nucleosome such as the H4 tail for ISWI and CHD1 and polyADP-ribosylation for ALC1 relieve this autoinhibition (*27*–*35*). Having the autoinhibition mechanism within the core ATPase may ensure that all complexes containing the ATPase subunit are subject to this regulation. By contrast, having the autoinhibition mechanism regulated by accessory subunits such as the Arp8 and Nhp10 modules may allow additional regulation of autoinhibition by the formation of subcomplexes.

### Implications for INO80's biological role in chromatin accessibility

The tight regulation of INO80 by flanking DNA length raises the question of why INO80 needs to be inhibited in sliding nucleosomes with ≤40 bp of DNA. Previous data have shown that once INO80 starts sliding nucleosomes, it rapidly moves nucleosomes by ~20 bp without re-sensing flanking DNA (*12*). This behavior contrasts with that of ISWI family remodelers that rapidly and bidirectionally move nucleosomes and re-sense flanking DNA after sliding nucleosomes by only ~3 bp (*36*). Therefore, the large conformational change identified here may represent a critical gating step, which ensures that rapid sliding only occurs when the flanking DNA is >40 bp. In the context of transcription, such regulation may be used to ensure that any movement of the +1 nucleosome into the gene body caused by other remodelers is rapidly reversed by moving the nucleosome toward the NDR (*37*). Consistent with this possibility, deletion of the Arp8 module perturbs spacing of the +1 nucleosome and other nucleosomes in the gene body (*38*). Deletion of the Arp8 module also exhibits defects in INO80-dependent regulation of transcription (*15*, *17*, *38*). These in vivo findings showcase the critical role of the Arp8 module in INO80's nucleosome positioning activity and provide a mechanistic explanation for why INO80 is essential for maintaining the positioning of the +1 nucleosome.

In addition to transcription, INO80 also plays important roles in DNA repair and replication (*37*). In the context of DNA repair, we propose that INO80's switch-like response ensures that the remodeler rapidly decreases nucleosome crowding to make DNA damage sites accessible. Deletions of the Arp8 module or the N terminus of Arp8 in yeast show sensitivity to replication stress and DNA damage (*15*, *17*). Additionally, another subunit of the Arp8 module, Ies4, has been shown to be phosphorylated by the Mec1/Tel1 kinases during exposure to DNA damage agents (*39*). These phosphorylation marks influence the DNA damage response, particularly when initiated by replicative stress. Although this region of Ies4 has not been observed by cryo-EM to date, it is possible that the interactions within the Arp8 module or with the rest of the complex are regulated by phosphorylation of Ies4. In comparison, phosphorylation of Arp8 has been shown to have larger effects on replication than transcription (*40*). Specifically, Arp8 is phosphorylated by the Dbf4-dependent kinase (DDK) within its unstructured N terminus at residues S65 and S233 (*40*). These phosphorylation sites lie in the negatively charged N terminus of Arp8 that we propose interacts with HSA to inhibit INO80's activity in a flanking DNA length–dependent manner. Disrupting phosphorylation of the N terminus of Arp8 widened the linker lengths between nucleosomes at replication origins, leading to replication defects with minimal changes in transcription (*40*). It is possible that phosphorylation of these sites in the N terminus of Arp8 tunes the interaction with Nhp10, and in turn the extent of autoinhibition as a function of flanking DNA length. It is also possible that phosphorylation of Arp8 more strongly tunes INO80's interactions with other factors at replication and not transcription sites. Overall, differential posttranslational modifications of the Arp8 module may regulate INO80's response to flanking DNA length in a context-dependent manner in yeast.

Most broadly, our findings showcase how a primitive nucleosome mobilization enzyme may have evolved into a sophisticated remodeler by the acquisition of modules that use nucleosome cues to impose restrictions on the remodeling output.

## Materials and methods

### Purification of INO80 complexes

To generate the ΔArp8 INO80 construct, the gene was deleted by knock-in at the endogenous locus in the *S. cerevisiae:* INO80-FLAG: S288C strain using a KanMX marker. The mutation was verified by colony polymerase chain reaction (PCR). The ΔArp8/Nhp10, Δ*N* – Arp8, and Arp8-AM constructs were cloned through a CRISPR-Cas9 system for *S. cerevisiae*. Briefly, guide RNAs (gRNAs, listed below) that targeted the N terminus of Arp8 were cloned into a plasmid carrying Cas9. The repair template was designed to have 100 bp of homology both upstream and downstream of the insert and ordered from TWIST biosciences. The guide RNA containing plasmid and repair template were transformed into the INO80-FLAG: S288C strain. The mutants were verified by PCR and sequencing of the locus.

gRNAs used to target the N terminus of Arp8:
1: 5′-GAGACACCCAGAAGTGTAAC-3′
2: 5′-ACAACTACTTTACCTGCCAC-3′
3: 5′-TAGCGTACCTTTAAGCAGCC-3′

The endogenous INO80 complexes were purified as previously reported (*12*). Briefly, 2x-FLAG tagged INO80 strains were grown at 30°C in YPD to saturation and harvested for purification. INO80 was purified by FLAG immunoprecipitation. The elution from FLAG immunoprecipitation was loaded onto a Mono Q 5/50 GL column and eluted by a linear salt gradient (100 mM KCl to 1 M KCl) over 20 column volumes. Peak fractions were dialyzed into storage buffer [25 mM Hepes (pH 7.5), 100 mM KCl, 10% glycerol, 1 mM EDTA, 1 mM DTT, and 0.02% NP-40].

### Nucleosome reconstitution

Recombinant *X. laevis* and *S. cerevisiae* histones were expressed in BL21(DE3) plysS cells and purified as previously described (*41*, *42*). 601 DNA was amplified from a plasmid containing the Widom 601 sequence and labeled with either a Cy3 or Cy5 fluorophore modified primer. The PCR products were separated on a 5% polyacrylamide gel and the desired band was cut out. The gel slice containing the DNA was crushed and soaked in 1X TE overnight and filtered through a 0.22-μm filer. The DNA was ethanol precipitated and dissolved in 1X TE. Refolding of histone octamers was performed as described previously. Nucleosomes were assembled using salt gradient dialysis and purified using a 10 to 30% glycerol gradient (*41*, *42*).

### Native gel-based remodeling assay

All remodeling reactions were done under single turnover conditions (enzyme in excess of nucleosomes) with saturating INO80. The reactions were carried out at either 10° or 30°C. Briefly, 40 nM WT INO80 was incubated with 10 nM nucleosomes in reaction buffer [26.5 mM Tris (pH 7.5), 13.5 mM Hepes (pH 7.5), 50 mM KCl, 7% glycerol, 0.01% NP-40, 1.1 mM $MgCl_2$] for 10 min. All remodeling reactions expect the ones shown in Fig. 3F were started with 1 mM ATP·$MgCl_2$. The remodeling reactions shown in Fig. 3F were started with 80 μM ATP· $MgCl_2$ to slow down *S.c* nucleosome remodeling at 30°C. The no ATP control was taken at the last time point of the reaction. The reaction samples taken at specific time points were quenched with excess plasmid DNA and ADP. Samples were resolved on a native PAGE gel (6% acrylamide, 0.5X TBE) ran for 3 to 4 hours at 125 V. Gels were scanned on a

Typhoon Imager (GE Life Sciences) and quantified by densitometry using ImageJ. All kinetics were performed in triplicates with more than one biological replicate. Using Prism 7 (GraphPad), data were fit to a single-phase exponential decay model (Eq. 1), where $y_0$ is the initial fraction product, $k_{obs}$ is the observed rate constant, and $p$ is the fraction product at the plateau.

$$y = (y_0 - p)e^{-k_{obs}t} + p$$

### Amine-functionalized GO grids preparation

Graphene oxide (GO) grids were prepared as previously described (*43*, *44*). Briefly, in a glass petri dish (60 mm in diameter, 15 mm in height) an epoxy coated stainless steel mesh stand was placed at the bottom and DI water was filled to the top. 300 Mesh, R1.2/1.3 Au Quantifoil grids were placed on the mesh stand with carbon side facing upward. Using a syringe, the GO solution (230 µl in total volume) was spread onto the water surface. After draining the water, the GO-coated grids were dried at room temperature for use. GO-covered grids were then submerged in 10 mM ethylenediamine solution diluted in dimethyl sulfoxide (DMSO) and incubated for 5 hours at room temperature. The grids were washed twice with DMSO without ethylenediamine, twice with autoclaved water, twice with ethanol, and dried under ambient conditions. Amino modified grids were stored dry at −20°C until use.

### Electron microscopy sample preparation and data collection

WT INO80 and nucleosomes (*X.l* 0/80, *X.l* 0/80, *S.c* 0/80, and *S.c* 0/40) were mixed in a 2:1 ratio and buffer exchanged into remodeling buffer [26.5 mM Tris (pH 7.5), 13.5 mM Hepes (pH 7.5), 50 mM KCl, 1.1 mM $MgCl_2$, and 1% glycerol] for 2 hours. After dialysis, the complex was incubated with 1 mM ADP, 1 mM $MgCl_2$, 1 mM $BeCl_2$, and 5 mM NaF at room temperature for 10 min. For the WT INO80–*S.c* 0/80 nucleosome sample in the apo state no nucleotide was added. ΔArp8 and ΔNhp10 INO80 were mixed in a 3:1 ratio with *S.c* 0/40 nucleosomes. All samples were prepared using functionalized GO-amine cryo-EM grids. Plunge freezing of the grids was carried out by applying 3 µL of sample at 8°C and 100% humidity on FEI Vitrobot IV with a wait time of 4 s, blot force of 0 using ø 55/20 mm blotting filter paper from TED PELLA.

All cryo-EM datasets were collected using SerialEM (*45*). Defocus range was set from -0.8 µm to −1.8 µm. For the dataset of WT INO80 bound to *X.l* 0/80 nucleosomes (ADP/$BeF_x$), 16,215 images were acquired with a nominal magnification of 105 K, resulting in a pixel size of 0.8189 Å. For the dataset of WT INO80 bound to *X.l* 0/40 nucleosomes (ADP/$BeF_x$), 8796 images were acquired with a nominal magnification of 105 K, resulting in a pixel size of 0.4155 Å. Each image was dose-fractionated to 50 frames, resulting in a total fluence of ~50 electrons per Å$^2$. Each image was dose-fractionated to 80 frames, resulting in a total fluence of ~47.7 electrons per Å$^2$. For the dataset of WT INO80 bound to *S.c* 0/80 nucleosomes (ADP/$BeF_x$), 11,890 images were acquired with a nominal magnification of 105 K, resulting in a pixel size of 0.835 Å. Each image was dose-fractionated to 80 frames, resulting in a total fluence of ~45.8 electrons per Å$^2$. For the dataset of WT INO80 bound to *S.c* 0/40 nucleosomes (ADP/$BeF_x$), 22,362 images were acquired with a nominal magnification of 105 K, resulting in a pixel size of 0.835 Å. Each image was dose-fractionated to 80 frames, resulting in a total fluence of ~45.8 electrons per Å$^2$. For the dataset of ΔNhp10 INO80 bound to *S.c* 0/40 nucleosomes (ADP/$BeF_x$), 8,740 images were acquired with a nominal magnification of 130 K, resulting in a pixel size of 0.940 Å. Each image was dose-fractionated to 2110 frames, resulting in a total fluence of ~60 electrons per Å$^2$. For the dataset of ΔArp8 INO80 bound to *S.c* 0/40 nucleosomes (ADP/$BeF_x$), 11,809 images were acquired with a nominal magnification of 105 K, resulting in a pixel size of 0.8189 Å. Each image was dose-fractionated to 80 frames, resulting in a total fluence of ~47.7 electrons per Å$^2$. For the dataset of WT INO80 bound to *S.c* 0/80 nucleosomes (Apo state), 9375 images were acquired with a nominal magnification of 105 K, resulting in a pixel size of 0.8189 Å. Each image was dose-fractionated to 80 frames, resulting in a total fluence of ~47.7 electrons per Å$^2$.

### Image processing

All datasets were processed using the same initial pipeline. In brief, movie stacks were motion-corrected and dose-weighted with MotionCor2 (*46*). The CTF parameters were estimated, and all subsequent 2D classification, heterogeneous refinement, and 3D classification were performed in cryoSPARC (*47*). The previously published cryo-EM map of the INO80 nucleosome complex (EMDB:28613) was used in cryoSPARC as a reference for template picking (*20*).

For the dataset of the WT INO80 *X.l*-0/80 sample in the ADP/$BeF_x$ state, a total of 2,385,551 particles were picked and extracted with a box size of 448x448 pixels centered at the middle of the particles. After 2D classification, heterogeneous refinement, and 3D classification, 109,876 particles with well-defined features of both the INO80 C-module and nucleosome were selected. Subsequent 3D volume analysis revealed density near the flanking DNA. To resolve this density, the selected particles were exported into RELION (*48*) and further auto-refined. These particles were then re-extracted with a box size of 360x360 pixels from the motion corrected micrographs centered at the flanking DNA. Further 3D classification identified a subset of 32,683 particles containing clear Arp8 module densities; focused refinement of Arp8 module yielded a 11.2 Å map. The same subset was extracted again with a box size of 448x448 pixels centered at the INO80 C-module. This subset of particles was imported back into cryoSPARC for nonuniform refinement, yielding a 2.6 Å map of the INO80 C-module and nucleosome. After, particle subtraction was applied to the same subset of particles to isolate the nucleosome with a box size of 240x240 pixels. Subsequent refinement using RELION and cisTEM yielded a nucleosome map with a resolution of 2.8 Å (*49*). Finally, the cryoSPARC map of the INO80 C-module, cisTEM map of the nucleosome and the RELION map of Arp8 module were assembled to generate a composite map.

For the dataset of WT INO80 bound to *X.l* 0/40 nucleosomes in the ADP/$BeF_x$ state, 1,543,010 particles were initially picked and extracted with a box size of 448x448 pixels centered at the middle of the particles. Following 2D classification, heterogeneous refinement, and 3D classification, a total of 30,914 particles with well-defined INO80 C-module and nucleosome features were selected. Subsequent 3D volume analysis revealed previously uncharacterized densities near the Ino80 RecA-lobes. To resolve this density, the selected particles were exported into RELION (*48*) and further auto-refined. These particles were then re-extracted with a box size of 320x320 pixels from the motion corrected micrographs centered at the Ino80 RecA-lobes. Further 3D classification identified a subset of 10,256 particles containing clear Arp8 module densities; focused refinement of Arp8 module yielded a 9.7 Å map. The same subset was extracted again with a box size of 448x448 pixels centered at the INO80 C-module. This subset of particles was imported back into cryoSPARC for nonuniform refinement, yielding a 3.3 Å map of the INO80 C-module and nucleosome. Finally, the cryoSPARC map of the INO80 C-module: nucleosome and the RELION map of Arp8 module were assembled to generate a composite map.

For the dataset of WT INO80 bound to the *S.c* 0/80 nucleosome in the apo state, a total of 1,721,659 particles were picked and extracted with a box size of 448x448 pixels centered at the middle of the particles. After 2D classification, heterogeneous refinement, and 3D classification, 41,849 particles with well-defined features of both the INO80 C-module and nucleosome were selected. Subsequent 3D volume analysis revealed density near the flanking DNA. To resolve this density, the selected particles were exported into RELION (*48*) and further auto-refined. These particles were then re-extracted with a box size of 360x360 pixels from the motion corrected micrographs centered at the flanking DNA. Further 3D classification identified a subset

of 17,836 particles containing clear Arp8 module densities; focused refinement of Arp8 module yielded a 14.7 Å map. The same subset was extracted again with a box size of 448x448 pixels centered at the INO80 C-module. This subset of particles was imported back into cryoSPARC for non-uniform refinement, yielding a 3.2 Å map of the INO80 C-module and nucleosome. Finally, the cryoSPARC map of the INO80 C-module: nucleosome and the RELION map of Arp8 module were assembled to generate a composite map.

For the dataset of WT INO80 bound to the *S.c* 0/80 nucleosome in the ADP/$BeF_x$ state, a total of 2,365,714 particles were picked and extracted with a box size of 448x448 pixels centered at the middle of the particles. After 2D classification and heterogeneous refinement, 721,488 particles were obtained with the INO80 C-module and nucleosome. To further improve the resolution, 3D classification was performed, yielding a final set of 138,910 particles that were subjected to non-uniform refinement in cryoSPARC to reconstruct the INO80 C-module and nucleosome complex with a global resolution of 2.9 Å.

For the dataset of WT INO80 bound to *S.c* 0/40 nucleosomes in the ADP/$BeF_x$ state, 3,625,796 particles were picked and extracted with a box size of 448x448 pixels centered at the middle of the particles. After 2D classification and heterogeneous refinement, 251,389 particles were selected. Subsequent 3D volume analysis revealed density near the Ino80 RecA-lobes and Arp5. To resolve these densities, the selected particles were exported to RELION (*48*) and further auto-refined. A mask containing the Arp5 module and the nucleosome was generated, followed by particle subtraction. Further 3D classification identified two well-defined classes that differed primarily in the grappler of Arp5: 74,790 particles in class 1 (the "parallel grappler") and 73,064 particles in class 2 (the "cross grappler"). The subtracted particles were reverted to their original form. These particles were then re-extracted with a box size of 320x320 pixels from the motion corrected micrographs centered at the Ino80 RecA-lobes. Further 3D classification identified a subset 32,763 particles in class 1 and 30,162 particles in class 2 containing clear Arp8 module densities; focused refinement of Arp8 module yielded a 8.4 Å and 8.6 Å map, respectively. The same subset was extracted again with a box size of 448x448 pixels centered at the INO80 C-module. This subset of particles was imported back into cryoSPARC for non-uniform refinement, yielding a 3.1 Å (class 1) and 3.2 Å (class 2) map of the INO80 C-module and nucleosome. Finally, the cryoSPARC map of the INO80 C-module: nucleosome and the RELION map of Arp8 module were assembled to generate a composite map.

For the dataset of ΔNhp10 INO80 bound to *S.c* 0/40 nucleosomes in the ADP/$BeF_x$ state, a total of 1,502,039 particles were picked and extracted with a box size of 480x480 pixels centered at the middle of the particles. After 2D classification and heterogeneous refinement, a final 101,622 particles with the INO80 C-module were obtained. Next, we imported this particle stack to RELION and performed particle subtraction to only contain the Ino80 RecA-lobes, Arp5, and the nucleosome with a box size of 240x240 pixels. Further 3D classification on the subtracted particles identified 40,107 particles with clear density for the Ino80 RecA-lobes, Arp5, and the nucleosome. These particles were refined in RELION and resulted in a 4.2 Å nucleosome map. The subtracted particles were then reverted to the original particles, and imported into cryoSPARC to preform nonuniform refinement, which resulted in 3.0 Å global map. We also re-extracted the particles with the Ino80 RecA-lobes as the center with a box size of 448x448 pixels. After 3D classification, 3,786 particles were identified with density that could partially contain the Arp8 module.

For the dataset of ΔArp8 INO80 bound to *S.c* 0/40 nucleosomes in the ADP/$BeF_x$ state, a total of 2,914,719 particles were picked and extracted with a box size of 448x448 pixels centered at the middle of the particles. After 2D classification and heterogeneous refinement, a final 159,734 particles were obtained for the INO80 C-module. Next, we imported this particle stack to RELION and performed particle subtraction to only include the nucleosome and Ino80 RecA-lobes with a box size of 240x240 pixels. Further 3D classification identified 36,091 particles with clear nucleosome density, resulting in a 4.2 Å nucleosome map. The subtracted particles were then reverted to the original particles, and imported into cryoSPARC to preform nonuniform refinement, which resulted in 2.9 Å global map.

To reduce classification bias, particles from all samples in the ADP/$BeF_x$ state (WT INO80–*X.l*-0/40, WT INO80–*X.l*-0/80, WT INO80–*S.c*-0/40, WT INO80–*S.c*-0/80, and ΔNhp10 INO80–*S.c*-0/40) were combined after initial particle selection in cryoSPARC. The combined dataset was then exported to RELION for global refinement, which revealed densities around both the Ino80 RecA-lobes and the flanking DNA. To resolve the density around the RecA-lobes or the flanking DNA, the particles were re-extracted with the center of the box shifted to RecA-lobes (320x320 pixels) or flanking DNA (360x360 pixels). These two sets of re-exacted particles are identical but centered differently. These particles were then subjected to 3D classification separately. The classification of particles centered at the RecA-lobes revealed two distinct classes: (i) clear density of the Arp8 module rotated ~180° away from the flanking DNA, and (ii) particles that did not contain clear density of the Arp8 module. The classification of particles centered at flanking DNA also revealed two distinct classes: (i) clear density of the Arp8 module bound to flanking DNA, and (ii) particles that did not contain clear density of the Arp8 module. Note that there is no overlap of particles in the classes with clearly defined Arp8 density from these two classifications. Together, this yielded three classes of particles: (i) the Arp8 module rotated away from flanking DNA, (ii) the Arp8 module bound to the flanking DNA, and (iii) undefined density for the Arp8 module. Particles of each class were then traced back to the original sample to calculate the ratio of particles between class 1 and 2. Subsequently, the particle sets corresponding to each sample were processed in RELION for 3D reconstruction. This confirmed that the distinct densities near the Ino80 RecA-lobes or bound to the flanking DNA remained after particles were reclassified into their respective datasets.

### Model building

For the model building, the initial model was generated by fitting the available coordinates into our cryo-EM density maps by using Chimera (*50*). These coordinates include the INO80 core (with its sequence changed to that of *S. cerevisiae* by Alphafold (*21*) and ccp4em), the model of the Arp8 module, the model of the *X.l* nucleosome, and the model of the *S.c* nucleosome (PDB: 6FML, 8A5O, 1KX5, and 1ID3) (*15*, *19*, *22*, *51*). The inconsistent parts were then manually built and refined in coot (*52*). The structures were refined using Phenix (*53*) with secondary structure constraints.

Summary of parameters used in data collection and model building are in tables S1 and S2.

### REFERENCES AND NOTES


1. M. R. Hübner, D. L. Spector, Chromatin dynamics. *Annu. Rev. Biophys.* **39**, 471–489 (2010). doi: 10.1146/annurev.biophys.093008.131348; pmid: 20462379
2. R. Bar-Ziv, Y. Voichek, N. Barkai, Chromatin dynamics during DNA replication. *Genome Res.* **26**, 1245–1256 (2016). doi: 10.1101/gr.201244.115; pmid: 27225843
3. K. Luger, A. W. Mäder, R. K. Richmond, D. F. Sargent, T. J. Richmond, Crystal structure of the nucleosome core particle at 2.8 A resolution. *Nature* **389**, 251–260 (1997). doi: 10.1038/38444; pmid: 9305837
4. M. Radman-Livaja, O. J. Rando, Nucleosome positioning: How is it established, and why does it matter? *Dev. Biol.* **339**, 258–266 (2010). doi: 10.1016/j.ydbio.2009.06.012; pmid: 19527704
5. K. Brogaard, L. Xi, J. P. Wang, J. Widom, A map of nucleosome positions in yeast at base-pair resolution. *Nature* **486**, 496–501 (2012). doi: 10.1038/nature11142; pmid: 22722846
6. T. N. Mavrich *et al.*, A barrier nucleosome model for statistical positioning of nucleosomes throughout the yeast genome. *Genome Res.* **18**, 1073–1083 (2008). doi: 10.1101/gr.078261.108; pmid: 18550805
7. E. A. Alcid, T. Tsukiyama, ATP-dependent chromatin remodeling shapes the long noncoding RNA landscape. *Genes Dev.* **28**, 2348–2360 (2014). doi: 10.1101/gad.250902.114; pmid: 25367034

8. N. Krietenstein *et al.*, Genomic Nucleosome Organization Reconstituted with Pure Proteins. *Cell* **167**, 709–721.e12 (2016). doi: 10.1016/j.cell.2016.09.045; pmid: 27768892
9. X. Shen, G. Mizuguchi, A. Hamiche, C. Wu, A chromatin remodelling complex involved in transcription and DNA processing. *Nature* **406**, 541–544 (2000). doi: 10.1038/35020123; pmid: 10952318
10. E. Oberbeckmann *et al.*, Genome information processing by the INO80 chromatin remodeler positions nucleosomes. *Nat. Commun.* **12**, 3231 (2021). doi: 10.1038/s41467-021-23016-z; pmid: 34050142
11. E. Oberbeckmann *et al.*, Ruler elements in chromatin remodelers set nucleosome array spacing and phasing. *Nat. Commun.* **12**, 3232 (2021). doi: 10.1038/s41467-021-23015-0; pmid: 34050140
12. C. Y. Zhou *et al.*, The Yeast INO80 Complex Operates as a Tunable DNA Length-Sensitive Switch to Regulate Nucleosome Sliding. *Mol. Cell* **69**, 677–688.e9 (2018). doi: 10.1016/j.molcel.2018.01.028; pmid: 29452642
13. M. Udugama, A. Sabri, B. Bartholomew, The INO80 ATP-dependent chromatin remodeling complex is a nucleosome spacing factor. *Mol. Cell. Biol.* **31**, 662–673 (2011). doi: 10.1128/MCB.01035-10; pmid: 21135121
14. A. Tosi *et al.*, Structure and subunit topology of the INO80 chromatin remodeler and its nucleosome complex. *Cell* **154**, 1207–1219 (2013). doi: 10.1016/j.cell.2013.08.016; pmid: 24034245
15. F. Kunert *et al.*, Structural mechanism of extranucleosomal DNA readout by the INO80 complex. *Sci. Adv.* **8**, eadd3189 (2022). doi: 10.1126/sciadv.add3189; pmid: 36490333
16. K. R. Knoll *et al.*, The nuclear actin-containing Arp8 module is a linker DNA sensor driving INO80 chromatin remodeling. *Nat. Struct. Mol. Biol.* **25**, 823–832 (2018). doi: 10.1038/s41594-018-0115-8; pmid: 30177756
17. S. Brahma, M. Ngubo, S. Paul, M. Udugama, B. Bartholomew, The Arp8 and Arp4 module acts as a DNA sensor controlling INO80 chromatin remodeling. *Nat. Commun.* **9**, 3309 (2018). doi: 10.1038/s41467-018-05710-7; pmid: 30120252
18. P. T. Lowary, J. Widom, New DNA sequence rules for high affinity binding to histone octamer and sequence-directed nucleosome positioning. *J. Mol. Biol.* **276**, 19–42 (1998). doi: 10.1006/jmbi.1997.1494; pmid: 9514715
19. S. Eustermann *et al.*, Structural basis for ATP-dependent chromatin remodelling by the INO80 complex. *Nature* **556**, 386–390 (2018). doi: 10.1038/s41586-018-0029-y; pmid: 29643509
20. H. Wu *et al.*, Reorientation of INO80 on hexasomes reveals basis for mechanistic versatility. *Science* **381**, 319–324 (2023). doi: 10.1126/science.adf4197; pmid: 37384669
21. J. Jumper *et al.*, Highly accurate protein structure prediction with AlphaFold. *Nature* **596**, 583–589 (2021). doi: 10.1038/s41586-021-03819-2; pmid: 34265844
22. C. L. White, R. K. Suto, K. Luger, Structure of the yeast nucleosome core particle reveals fundamental changes in internucleosome interactions. *EMBO J.* **20**, 5207–5218 (2001). doi: 10.1093/emboj/20.18.5207; pmid: 11566884
23. S. Ray, A. Grove, The yeast high mobility group protein HMO2, a subunit of the chromatin-remodeling complex INO80, binds DNA ends. *Nucleic Acids Res.* **37**, 6389–6399 (2009). doi: 10.1093/nar/gkp695; pmid: 19726587
24. C. Y. Zhou, S. L. Johnson, N. I. Gamarra, G. J. Narlikar, Mechanisms of ATP-Dependent Chromatin Remodeling Motors. *Annu. Rev. Biophys.* **45**, 153–181 (2016). doi: 10.1146/annurev-biophys-051013-022819; pmid: 27391925
25. J. G. Yang, T. S. Madrid, E. Sevastopoulos, G. J. Narlikar, The chromatin-remodeling enzyme ACF is an ATP-dependent DNA length sensor that regulates nucleosome spacing. *Nat. Struct. Mol. Biol.* **13**, 1078–1083 (2006). doi: 10.1038/nsmb1170; pmid: 17099699
26. I. Whitehouse, C. Stockdale, A. Flaus, M. D. Szczelkun, T. Owen-Hughes, Evidence for DNA translocation by the ISWI chromatin-remodeling enzyme. *Mol. Cell. Biol.* **23**, 1935–1945 (2003). doi: 10.1128/MCB.23.6.1935-1945.2003; pmid: 12612068
27. A. J. Gottschalk, R. D. Trivedi, J. W. Conaway, R. C. Conaway, Activation of the SNF2 family ATPase ALC1 by poly(ADP-ribose) in a stable ALC1·PARP1·nucleosome intermediate. *J. Biol. Chem.* **287**, 43527–43532 (2012). doi: 10.1074/jbc.M112.401141; pmid: 23132853
28. A. J. Gottschalk *et al.*, Poly(ADP-ribosyl)ation directs recruitment and activation of an ATP-dependent chromatin remodeler. *Proc. Natl. Acad. Sci. U.S.A.* **106**, 13770–13774 (2009). doi: 10.1073/pnas.0906920106; pmid: 19666485
29. L. C. Lehmann *et al.*, Mechanistic Insights into Autoinhibition of the Oncogenic Chromatin Remodeler ALC1. *Mol. Cell* **68**, 847–859.e7 (2017). doi: 10.1016/j.molcel.2017.10.017; pmid: 29220652
30. H. R. Singh *et al.*, A Poly-ADP-Ribose Trigger Releases the Auto-Inhibition of a Chromatin Remodeling Oncogene. *Mol. Cell* **68**, 860–871.e7 (2017). doi: 10.1016/j.molcel.2017.11.019; pmid: 29220653
31. G. Hauk, J. N. McKnight, I. M. Nodelman, G. D. Bowman, The chromodomains of the Chd1 chromatin remodeler regulate DNA access to the ATPase motor. *Mol. Cell* **39**, 711–723 (2010). doi: 10.1016/j.molcel.2010.08.012; pmid: 20832723
32. I. M. Nodelman, Z. Shen, R. F. Levendosky, G. D. Bowman, Autoinhibitory elements of the Chd1 remodeler block initiation of twist defects by destabilizing the ATPase motor on the nucleosome. *Proc. Natl. Acad. Sci. U.S.A.* **118**, e2014498118 (2021). doi: 10.1073/pnas.2014498118; pmid: 33468676
33. J. D. Leonard, G. J. Narlikar, A nucleotide-driven switch regulates flanking DNA length sensing by a dimeric chromatin remodeler. *Mol. Cell* **57**, 850–859 (2015). doi: 10.1016/j.molcel.2015.01.008; pmid: 25684208
34. C. R. Clapier, B. R. Cairns, Regulation of ISWI involves inhibitory modules antagonized by nucleosomal epitopes. *Nature* **492**, 280–284 (2012). doi: 10.1038/nature11625; pmid: 23143334
35. N. Gamarra, S. L. Johnson, M. J. Trnka, A. L. Burlingame, G. J. Narlikar, The nucleosomal acidic patch relieves auto-inhibition by the ISWI remodeler SNF2h. *eLife* **7**, e35322 (2018). doi: 10.7554/eLife.35322; pmid: 29664398
36. T. R. Blosser, J. G. Yang, M. D. Stone, G. J. Narlikar, X. Zhuang, Dynamics of nucleosome remodelling by individual ACF complexes. *Nature* **462**, 1022–1027 (2009). doi: 10.1038/nature08627; pmid: 20033040
37. J. Poli, S. M. Gasser, M. Papamichos-Chronakis, The INO80 remodeller in transcription, replication and repair. *Philos. Trans. R. Soc. Lond. B Biol. Sci.* **372**, 20160290 (2017). doi: 10.1098/rstb.2016.0290; pmid: 28847827
38. A. K. Singh, T. Schauer, L. Pfaller, T. Straub, F. Mueller-Planitz, The biogenesis and function of nucleosome arrays. *Nat. Commun.* **12**, 7011 (2021). doi: 10.1038/s41467-021-27285-6; pmid: 34853297
39. A. J. Morrison *et al.*, Mec1/Tel1 phosphorylation of the INO80 chromatin remodeling complex influences DNA damage checkpoint responses. *Cell* **130**, 499–511 (2007). doi: 10.1016/j.cell.2007.06.010; pmid: 17693258
40. S. L. Priyanka Bansal *et al.*, Dbf4-Dependent Kinase Finetunes INO80 Function at Chromosome Replication Origins. *bioRxiv*, (2024).
41. P. N. Dyer *et al.*, Reconstitution of nucleosome core particles from recombinant histones and DNA. *Methods Enzymol.* **375**, 23–44 (2004). doi: 10.1016/S0076-6879(03)75002-2; pmid: 14870657
42. K. Luger, T. J. Rechsteiner, T. J. Richmond, Expression and purification of recombinant histones and nucleosome reconstitution. *Methods Mol. Biol.* **119**, 1–16 (1999). doi: 10.1385/1-59259-681-9:1; pmid: 10804500
43. E. Palovcak *et al.*, A simple and robust procedure for preparing graphene-oxide cryo-EM grids. *J. Struct. Biol.* **204**, 80–84 (2018). doi: 10.1016/j.jsb.2018.07.007; pmid: 30017701
44. F. Wang *et al.*, Amino and PEG-amino graphene oxide grids enrich and protect samples for high-resolution single particle cryo-electron microscopy. *J. Struct. Biol.* **209**, 107437 (2020). doi: 10.1016/j.jsb.2019.107437; pmid: 31866389
45. D. N. Mastronarde, Automated electron microscope tomography using robust prediction of specimen movements. *J. Struct. Biol.* **152**, 36–51 (2005). doi: 10.1016/j.jsb.2005.07.007; pmid: 16182563
46. S. Q. Zheng *et al.*, MotionCor2: Anisotropic correction of beam-induced motion for improved cryo-electron microscopy. *Nat. Methods* **14**, 331–332 (2017). doi: 10.1038/nmeth.4193; pmid: 28250466
47. A. Punjani, J. L. Rubinstein, D. J. Fleet, M. A. Brubaker, cryoSPARC: Algorithms for rapid unsupervised cryo-EM structure determination. *Nat. Methods* **14**, 290–296 (2017). doi: 10.1038/nmeth.4169; pmid: 28165473
48. S. H. Scheres, RELION: Implementation of a Bayesian approach to cryo-EM structure determination. *J. Struct. Biol.* **180**, 519–530 (2012). doi: 10.1016/j.jsb.2012.09.006; pmid: 23000701
49. T. Grant, A. Rohou, N. Grigorieff, *cis*TEM, user-friendly software for single-particle image processing. *eLife* **7**, e35383 (2018). doi: 10.7554/eLife.35383; pmid: 29513216
50. E. F. Pettersen *et al.*, UCSF Chimera—A visualization system for exploratory research and analysis. *J. Comput. Chem.* **25**, 1605–1612 (2004). doi: 10.1002/jcc.20084; pmid: 15264254
51. C. A. Davey, D. F. Sargent, K. Luger, A. W. Maeder, T. J. Richmond, Solvent mediated interactions in the structure of the nucleosome core particle at 1.9 a resolution. *J. Mol. Biol.* **319**, 1097–1113 (2002). doi: 10.1016/S0022-2836(02)00386-8; pmid: 12079350
52. P. Emsley, K. Cowtan, Coot: Model-building tools for molecular graphics. *Acta Crystallogr. D Biol. Crystallogr.* **60**, 2126–2132 (2004). doi: 10.1107/S0907444904019158; pmid: 15572765
53. P. V. Afonine *et al.*, Towards automated crystallographic structure refinement with phenix.refine. *Acta Crystallogr. D Biol. Crystallogr.* **68**, 352–367 (2012). doi: 10.1107/S0907444912001308; pmid: 22505256



## ACKNOWLEDGMENTS

The Cryo-EM facility at UCSF is managed by D. Bulkley and G. Gilbert. Computation at Cheng laboratory is supported by M. Harrington and C. Li. We thank F. Wang an Y. Chen for providing GO grids, J. Tretyakova for expressing and purifying histones, M. Huang for help with generating the Arp8 mutants, and members of Narlikar and Cheng laboratories for helpful discussions. We thank L. Hsieh for making the ΔArp8 INO80 strain and performing studies of ΔArp8 INO80 on *X.l* nucleosomes, which influenced the work done here. We thank C. Wu and A. Rajan for providing the *S.c* H4 plasmid and help with the purification. **Funding:** This work is supported by grants from National Institute of Health (1R35GM140847 to Y.C., R35 GM127020 to G.J.N.). Equipment at the UCSF cryo-EM facility was partially supported by National Institutes of Health (NIH) grants (S10OD020054, S10OD021741, and S10OD025881).

Y.C. is an Investigator of Howard Hughes Medical Institute. **Author contributions:** U.K. purified all INO80 complexes and nucleosome substrates. U.K. performed and quantified all biochemical experiments. U.K. prepared cryo-EM samples. H.W. collected cryo-EM data. H.W. processed the cryo-EM data and built the models with assistance from U.K. G.J.N. and Y.C. oversaw the project. All authors participated in interpretation and discussion of the results and writing of the manuscript. **Competing interests:** G.J.N is a co-founder of TippingPoint Biosciences. Y.C. is on the scientific advisory boards of ShuiMu BioSciences Ltd. and Pamplona Therapeutics. **Data and materials availability:** For *S.c.* INO80 bound to *X.l.* 0/40 nucleosomes, *S.c.* 0/80 nucleosomes and *S.c.* 0/40 nucleosomes (class 1 and class 2), the coordinates are deposited in the Protein Data Bank (PDB) with the accession codes 9CAN, 9C9G, 9C9S, and 9C9T; the cryo-EM density maps are deposited in the Electron Microscopy Data Bank (EMDB) with the accession codes EMD-45397, EMD-45361, EMD-45369, and EMD-45370. For the INO80 C-module of *S.c.* WT INO80 bound to *X.l.* 0/80 nucleosomes, ΔArp8 INO80 bound to *S.c.* 0/40 nucleosomes, ΔNhp10 INO80 bound to *S.c.* 0/40 nucleosomes, the coordinates are deposited in PDB with the accession codes 9C9Z, 9CAT, and 9CCD, the cryo-EM density maps are deposited in EMDB with the accession codes EMD-45377, EMD-45403, and EMD-45441. For the nucleosome or Ino80-nucleosome of *S.c.* INO80 bound to *X.l.* 0/80 nucleosomes, ΔArp8 INO80 bound to *S.c.* 0/40 nucleosomes, ΔNhp10 INO80 bound to *S.c.* 0/40 nucleosomes, the coordinates are deposited in PDB with the accession codes 9C9X, 9CAU, and 9CB7, the cryo-EM density maps are deposited in the EMDB with the accession codes EMD-45375, EMD-45404, and EMD-45418. The Arp8 mutant yeast strains will be available upon request. 

## SUPPLEMENTARY MATERIALS

science.org/doi/10.1126/science.adr3831
Figs. S1 to S18; Tables S1 and S2; MDAR Reproducibility Checklist; Movie S1
Submitted 9 July 2024; resubmitted 7 March 2025; accepted 2 May 2025
10.1126/science.adr3831